Design and modeling of asymmetric bow-tie VCSELs for 100 GHz and beyond

Research Article Vol. 34, No. 5 / 9 Mar 2026 / Optics Express 7979
Optics EXPRESS

Design and modeling of asymmetric bow-tie VCSELs for 100 GHz and beyond

M. D'Alessandro,[1,2] V. Torrelli,[1,2,*] A. Gullino,[2] M. G. C. Alasio,[1,2] A. Nespola,[3] S. Romero García,[4] and P. Debernardi[2]

[1]*Department of Electronics and Telecommunications (DET), Politecnico di Torino, Corso Duca degli Abruzzi, 24, 10129, Torino, Italy*
[2]*Istituto di Elettronica e di Ingegneria dell'Informazione e delle Telecomunicazioni (IEIIT) del Consiglio Nazionale delle Ricerche (CNR), Corso Duca degli Abruzzi,24, 10129, Torino, Italy*
[3]*LINKS Foundation, Via Pier Carlo Boggio, 61, 10138 Torino, Italy*
[4]*Cisco Optical, Nuremberg, Germany*
[*]*valerio.torrelli@polito.it*

Abstract: We present the design and numerical analysis of an asymmetric bow-tie vertical-cavity surface-emitting laser (ABT-VCSEL) that enables PAM-2 direct modulation up to 100 GHz. The device concept relies on photon-photon resonance (PPR) between laterally coupled modes, triggered by a structural asymmetry introduced via a hollowed dielectric mirror. This approach avoids the need for asymmetric pumping and probing while ensuring strong modal coupling under uniform carrier injection. A dynamical in-house suite, combining field-carrier interaction, electromagnetic, and thermal problems, is developed and discussed to evaluate device performance under realistic conditions. The simulation results predict a 3-dB bandwidth up to 70 GHz with low modulation swing, and open eye diagrams at 100 GHz PAM-2 modulation and 70 GHz PAM-4 modulation. The proposed ABT-VCSEL concept shows robustness against geometrical variations and ambient temperature when proper cavity detuning is applied, making it a promising candidate for next-generation ultra-fast short-reach interconnects.

1. Introduction

Vertical-cavity surface-emitting lasers (VCSELs) are key light sources for short-reach interconnects, as they combine high modulation speed, compactness, and low energy per bit, enabling cost and power-efficient optical links [1–4].

Traditional bandwidth improvement strategies focus on optimizing photon lifetime, working on optical and carrier confinement, mitigating self-heating, and minimizing carrier transport delays [5–8]. Although effective, these approaches face unavoidable trade-offs [9]. At present, the maximum achievable small-signal bandwidth is around 40 GHz [10,11], which, combined with advanced modulation schemes, can reach optical transmission rates of 200 Gbps [12–15]. To overcome this limit, unconventional strategies are being explored, such as spin-VCSELs [16], integrated electro-optic modulators [17] and transverse coupled-cavity (TCC) VCSELs [18–21].

The latter approach leverages the combined resonance of laterally coupled elements to enhance the bandwidth through the concept of photon-photon resonance (PPR) [22]. Our theoretical study in [23] describes the physics of these devices using the scalar wave equation. Its predictions are compared with experiments in [24] to interpret coherent emission in a two-apertures TCC VCSEL, and in [25] to fit recent observations [20]. The results of [23] show that symmetric *bow-tie* (BT) devices, *i.e.*, consisting of two coupled apertures of identical size [26], can provide PPR only if the symmetry is broken by partial probing of the light and asymmetric carrier pumping. However, this requires complex double contacting [18] and partial optical probing [27], which are unattractive for industrial applications.

#578425 https://doi.org/10.1364/OE.578425
Journal © 2026 Received 10 Sep 2025; revised 24 Oct 2025; accepted 26 Oct 2025; published 26 Feb 2026

Optics EXPRESS

For this reason, this work investigates an alternative approach, which consists of introducing a structural asymmetry to avoid the complicated pumping and probing scheme. To do so, we firstly introduced a partial metallization at the outcoupling facet covering one of the two apertures, which however resulted in a major drop of outcoupling efficiency of the lasing mode, becoming as low as $1 \div 10\%$ for current values that are interesting for high-speed modulation. For this reason, we opted to break the symmetry by covering one of the two apertures with a dielectric mirror. This geometry leads to the non-orthogonality of the modes in the active region (AR), enabling mode coupling under uniform carrier pumping and ultimately enhancing the modulation bandwidth, as detailed in the following.

The analysis is conducted using a novel framework, which combines thermal simulations [28], an electromagnetic modal solver [29,30], a distributed rate-equation model [24,31] and an optical gain model [32]. The presented method accounts for both self-heating and structural variations of the nominal design, which have a major impact on the investigated device.

The article is structured as follows: in Section 2, we describe the VCSEL designs under investigation. Section 3 outlines the simulation methodologies. Section 4 presents the results, and in Section 5 we draw our conclusions.

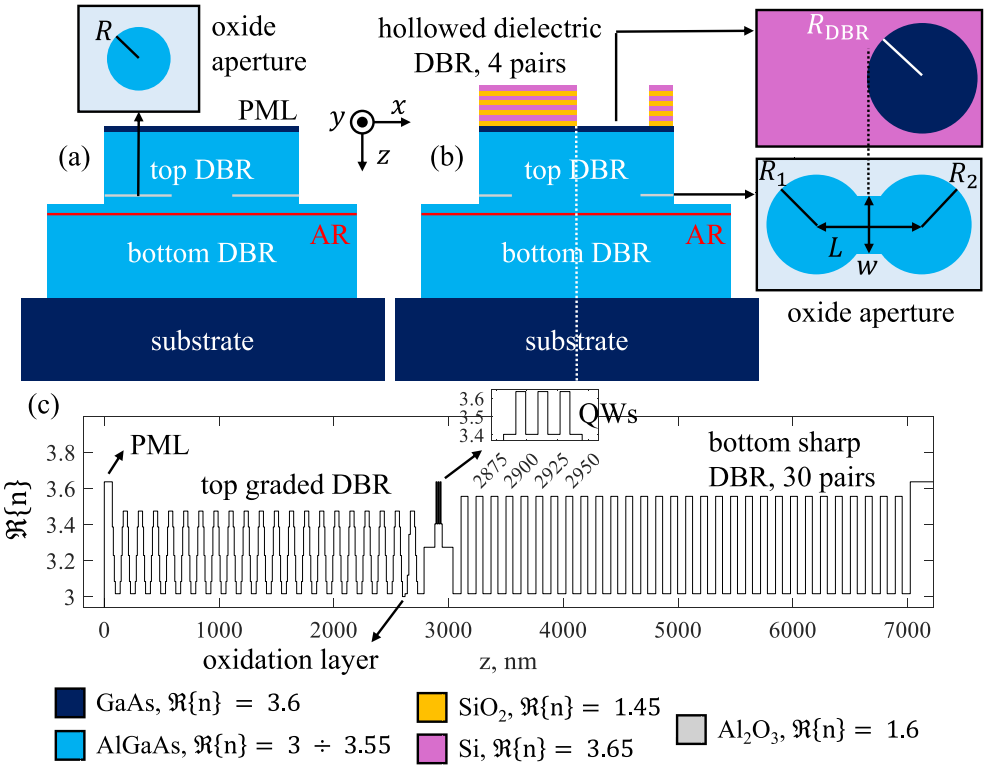

Fig. 1. (a) Schematic of the circular VCSEL. The inset represents the oxide aperture transverse shape. (b) Schematic of the proposed ABT-VCSEL, with the hollowed dielectric DBR on top of the PML. Insets show the oxide aperture and the circular hole in the dielectric DBR. (c) Longitudinal refractive index profile for the circular VCSEL. We highlight the PML, the AR with the relative QWs and the oxidation layer.

Optics EXPRESS

2. Asymmetric bow-tie VCSEL: concept and design

The considered geometry is the one realized in [33] for an 850 nm circular VCSEL, serving as a reference device, consisting of a λ–cavity with three GaAs 8 nm quantum wells (QWs) sandwiched between a bottom and a top distributed Bragg reflector (DBR). The corresponding longitudinal refractive index is reported in Fig. 1(c).

We design and numerically investigate a BT-VCSEL, intentionally breaking its symmetry. The simulation results show that this configuration allows for bandwidth enhancement without asymmetric pumping and probing [23]. As sketched in Fig. 1(b), this is realized by growing on top of a BT-VCSEL a hollowed dielectric DBR, aligning its hole to the right aperture. Such DBR features four $\lambda/4$ pairs for optimal reflectivity. From a manufacturing standpoint, it can be realized by sputtering via inductively coupled plasma chemical vapor deposition (ICPCVD) as in [34]. We will refer to this new concept as the asymmetric bow-tie VCSEL (ABT-VCSEL). The ABT-VCSEL features the same epitaxial structure as our reference circular VCSEL of Fig. 1(a), only differing in the number of top DBR pairs, reduced from 20 to 17. In this way the ABT and circular VCSELs features similar threshold gain, which is useful for performance comparison.

Referring to Fig. 1(c), for the ABT-VCSEL we adopt a bow-tie featuring $R_1 = R_2 = 1.5\ \mu$m, $L = 3.9\ \mu$m, and $w = 1.2\ \mu$m, as in [26]. The dielectric DBR hole ($R_{\mathrm{DBR}} = 2\ \mu$m) is aligned such that the leftmost edge of the circle coincides with the center of the BT, as shown in the insets in Fig. 1(b). The radius of the circular VCSEL is set to $R = 2.2\ \mu$m, so that the two apertures have the same area. Notice how, in Fig. 1, the phase matching layer (PML) is highlighted for both structures, as its thickness greatly impacts on the dynamical performances.

3. Modeling

In this section we introduce our simulation framework, which we use to evaluate relevant figures of merit in static and dynamic operation, for the circular and ABT-VCSELs. In its first version [23], the model consisted of a lumped system of four dynamical equations. Later, it has been updated to a distributed model accounting for the carrier diffusion equation [24,31].

In this work, we incorporate self-heating and power rollover together with a realistic material gain, thus avoiding the commonly adopted linearized expression [35]. The QW gain g is computed using a Fermi golden rule approach [32], which accounts for its dependence on wavelength, temperature, and carrier density. Fig. 2 reports the gain g as a function of carrier density N, at varying wavelength and temperature.

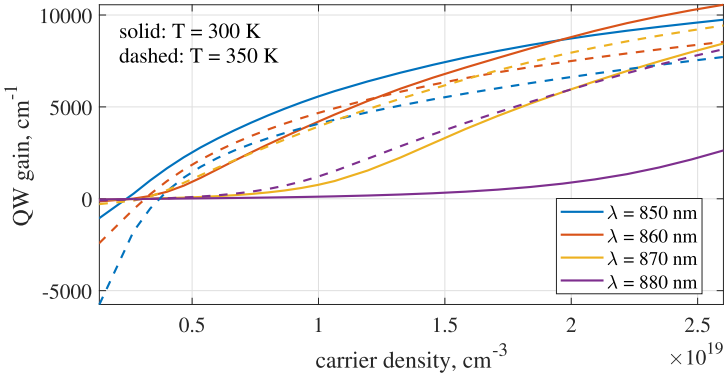

Fig. 2. Material gain produced by an 8 nm thick GaAs QW as a function of carrier density, wavelength and temperature.

Our heat equation solver [28] computes the temperature variations starting from a given distribution of heat sources, the latter depending on the bias point. The estimation of a realistic

Optics EXPRESS

temperature profile is a crucial aspect in the modeling of high-speed devices, since self-heating is a major limiting factor for datacom performance [7]. The resulting self-heating profile is then given as an input to our in-house VCSEL modal solver VELMS [29] together with the 3-dimensional refractive index profile.

VELMS provides modal shape, threshold gain, and emission wavelength for each computed mode. Finally, for a given bias point, the parameters computed by the optical solver, together with the QW gain, are provided as inputs to the dynamical solver. The dynamical model [24,31] consists of a distributed rate equation system that computes the 2-dimensional spatial distribution of carriers in the AR, self-consistently with the optical problem, ultimately accounting for spatial hole burning [35].

All of our software is run on a standard PC, and is implemented so that an entire simulation, from the solution of the heat equation up to the computation of the bandwidth, runs in few minutes.

3.1. Optical solver

The foundations of our in-house optical solver VELMS are outlined in [29,30]. VELMS determines the supported transverse modes of the various geometries. It requires as input the VCSEL 3D refractive index, which defines the optical resonator. The self-heating temperature profile is converted into a refractive index variation to the cold-cavity index distribution. In this way, the impact of geometrical variations is explored alongside the effects of temperature on the modal features. By exploiting the direct relationship between current and temperature, at each current we are able to calculate all modal features, for each investigated geometry.

For each i-th transverse mode, VELMS returns its emission wavelength λ_i, QW threshold gain $G_{\text{th}}^{(i)}$, electric field distribution $E_i(x, y, z)$ with relative transverse profile $\Psi_i(x, y)$ at the central QW, longitudinal Poynting vector $S_z^{(i)}(x, y, z)$ and longitudinal confinement factor Γ_z. The latter in our structure is $\Gamma_z \simeq 0.042$. The emission wavelength is converted into optical pulsation as $\omega_i = 2\pi c/\lambda_i$ (c being the speed of light), while the threshold gain is related to photon lifetime by:

$$\tau_p^{(i)} = \frac{1}{G_{\text{th}}^{(i)} v_g \Gamma_z}, \tag{1}$$

where v_g is the group velocity. By choosing as reference pulsation $\bar{\omega}$ that of the fundamental mode, we introduce the quantity $\Delta\omega_i = \omega_i - \bar{\omega}$, which will be needed in the dynamical model. Let us also recall that the amplitude modal loss α_i is related to photon lifetime by $\alpha_i = (2\tau_p^{(i)})^{-1}$.

The modal outcoupling efficiency η_i is obtained through the Poynting vector. In Fig. 3, we report $P(z) = \Re\{S_z(z)\}$ for the 1D optical simulation related to the VCSEL longitudinal index profile of Fig. 1(c). The regions where $P(z)$ is not constant are governed by losses, which enter the model as the imaginary part of the refractive index. In our structure, the considered losses are $8 \cdot 10^3\,\text{cm}^{-1}$ in the highly absorbing GaAs PML, and $10\,\text{cm}^{-1}$ and $3\,\text{cm}^{-1}$ in the top and bottom DBRs, respectively. These values are taken from [32] and account for free-carrier absorption. Defining ΔP as the QW gain induced power jump of $P(z)$ and P_{out} as $P(z)$ at the output facet as reported in Fig. 3, the 1D outcoupling efficiency η is defined as:

$$\eta = \frac{P_{\text{out}}}{\Delta P}, \tag{2}$$

and represents the ratio between the power exiting the device and the power generated by the QWs. In a 3D case, the definition is identical when defining $P(z)$ as the integral of the Poynting vector over the transverse plane, which is actually what we do in our model (see Fig. 8).

Optics EXPRESS

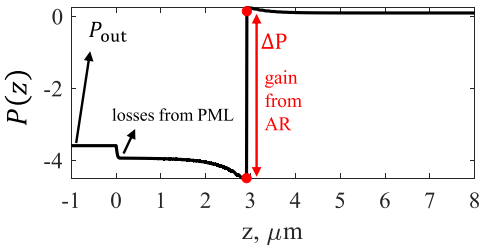

Fig. 3. $P(z)$ in the circular case obtained in a 1D simulation, highlighting the needed quantities to evaluate the outcoupling efficiency, *i.e.*, ΔP and P_{out}. Notice how $P_{\text{out}}<0$, as power exits from the left.

3.2. Dynamical solver

Our dynamical solver uses as input the modal parameters obtained from the thermal, optical and gain modules, and evaluates the relevant dynamical characteristics, including the light-current (LI) curves, the intensity-modulation (IM) response and the eye diagrams.

Starting from the scalar wave equation [36] and applying the slowly varying envelope approximation, the unknown time-varying electric field is expressed as a superposition of the supported steady-state VCSEL modes, resulting in a set of coupled ordinary differential equations that describe the time evolution of the complex expansion coefficients [23]. Since the derivation relies on the scalar wave equation, the optical modes are treated within the linearly polarized (LP) approximation [29]. Conventionally, we use E_x, H_y, being (x, y) the transverse plane and z the longitudinal axis, as indicated in Fig. 1. Coupling the field dynamical equations with the carrier diffusion equation yields a closed system whose input is the injected current distribution in the AR across the transverse plane, assumed to be constant within the oxide aperture.

Our dynamical system reads:

$$\frac{de_i(t)}{dt} = (-\alpha_i + \mathrm{i}\Delta\omega_i)\, e_i(t) + \sum_{j=1}^{M} k_{ij}(t) e_j(t), \qquad i = 1, \ldots, M, \tag{3}$$

$$\frac{\partial N(x,y,t)}{\partial t} = -R(N) - v_g \Re\{\tilde{g}\} S(x,y,t) + I(t)\frac{\mathcal{T}(N) P_{\text{ox}}(x,y)}{qV_{\text{act}}} + D\nabla^2 N, \tag{4}$$

where i is the imaginary unit and M is the number of considered transverse modes. After solving (3)–(4), it is shown in the Supplement 1 that the output optical power in a bimodal case ($M = 2$) is obtained as a post-processing of the expansion coefficients $e_i(t)$:

$$P(t) = 2E_{\text{ph}} L_{\text{opt}} \left\{ \eta_1 \alpha_1 |e_1(t)|^2 + \eta_2 \alpha_2 |e_2(t)|^2 - \sqrt{\eta_1 \eta_2}\, \Re\left\{ \frac{d\left[e_1^*(t) e_2(t)\right]}{dt} \xi_{12} \right\} \right\}. \tag{5}$$

In the following, we define all of the quantities in (3), (4) and (5).

$$\xi_{12} = \iint_{\mathbb{R}^2} \Psi_1^* \Psi_2 \, \mathrm{d}x\mathrm{d}y \tag{6}$$

is the overlap integral, E_{ph} is the photon energy at the operation wavelength and $L_{\text{opt}} = N_{\text{QW}} d_{\text{QW}} / \Gamma_z$ represents the optical length. The unknowns $e_i(t)$ of (3) are the time-varying expansion coefficients

Optics EXPRESS

of the time-varying electric field $\mathcal{E}$ in the AR:

$$\mathcal{E}(x,y,t) = \sum_{i=1}^{M} e_i(t)\Psi_i(x,y). \tag{7}$$

The coupling coefficients k_{ij}

$$k_{ij}(t) = \frac{v_g \Gamma_z}{2} \iint_{\mathbb{R}^2} \Psi_i^*(x,y)\, \tilde{g}(x,y,t)\, \Psi_j(x,y)\, \mathrm{d}x\mathrm{d}y \tag{8}$$

introduce the PPR coupling in our model, via the cross projection on the modal profiles of the total complex gain $\tilde{g}$, which reads:

$$\tilde{g}(x,y,t) = \frac{1 + i\alpha_{\mathrm{H}}}{1 + \epsilon_{\mathrm{nlg}} S(x,y,t)}\, g(N(x,y,t)), \tag{9}$$

where $N(x,y,t)$ is the carrier density in the AR, α_{H} the linewidth enhancement factor, ϵ_{nlg} the spectral hole burning non-linear coefficient, and $S(x,y,t)$ the photon density, defined as

$$S(x,y,t) = \left| \sum_{i=1}^{M} e_i(t)\Psi_i(x,y) \right|^2. \tag{10}$$

The carrier diffusion Eq. (4) governs the spatio-temporal evolution of N, where $R(N)$ represents carrier recombination, $I(t)$ the injected current, q the elementary charge, and D the carrier diffusion coefficient. The dimensionless carrier-dependent coefficient $\mathcal{T}(N)$ mimics the injection efficiency in the QWs:

$$\mathcal{T}(N) = \{1 + \exp[(N - N_1)/N_2]\}^{-1}, \tag{11}$$

where N_1 and N_2 represent phenomenological parameters, describing a maximum carrier density in the QWs. This is fundamental to reproduce reasonable roll-over conditions. The function $P_{\mathrm{ox}}(x,y)$ defines the oxide-shaped port function and, finally, the active volume is given by

$$V_{\mathrm{act}} = N_{\mathrm{QW}} d_{\mathrm{QW}} A_{\mathrm{ox}}, \tag{12}$$

with N_{QW} the number of QWs, d_{QW} the QW thickness, and A_{ox} the oxide aperture area.

The nominal values for all of the parameters that are not obtained from optical simulations are reported in Table 1, and are tailored so that the bandwidth of the single-mode circular device is comparable with the current state of the art [10,11].

3.3. Thermal solver

Self-heating is induced by several phenomena related to the injected current, such as Joule effect, capture heating from the barriers to the QWs, non-radiative recombination and optical absorption [32].

Our suite exploits the direct relation between temperature and current derived from our steady-state electro-thermal-optical VENUS code applied to the circular reference VCSEL [32,37], as reported in Fig. 7(i). This is used to update, at each current, the modal parameters, which are influenced by the thermal lensing, and the QW gain. A major effect is the gain deterioration due to its temperature-induced wavelength shift, which causes a misalignment with respect to the resonant frequency. For this reason, the threshold carrier density increases, until it approaches the maximum occupancy level introduced in (11). The combination of these effects give rise to a power roll-over. Furthermore, an accurate estimation of the spatial temperature distribution is essential, as it directly impacts the modal characteristics in three distinct ways [24]: the frequency

Optics EXPRESS

Table 1. List of parameters used in the simulations.

Symbol	Value	Description
κ_{air}	0.025 W/m/K	Air thermal conductivity
$\kappa_{\text{substrate}}$	41.4 W/m/K	Substrate thermal conductivity
$\kappa_{p,\text{VCSEL}}$	13.5 W/m/K	VCSEL transverse thermal conductivity
$\kappa_{z,\text{VCSEL}}$	9.7 W/m/K	VCSEL longitudinal thermal conductivity
$\kappa_{\text{passivation}}$	0.025 W/m/K	Passivation thermal conductivity
v_g	8.33×10^7 m/s	Group velocity
N_1	6×10^{18} cm^{-3}	Parameter for the limited injection efficiency
N_2	1×10^{18} cm^{-3}	Parameter for the limited injection efficiency
T_a	300 K	Ambient temperature
α_{H}	2	Linewidth enhancement factor
ϵ_{nlg}	1.75×10^{23} m^3	Spectral hole burning coefficient
τ_n	1 ns	Carrier lifetime
D	0.025 m^2/s	Carrier diffusivity

spacing and the modal overlap increase, and the modal profile undergo thermally induced lensing toward the device center. The static heat equation in the VCSEL is solved with a numerically efficient in-house finite element solver, following the approach described in [28,38], with a spatial domain that must comprise the entire mesa and passivation volumes, which are much larger than the heat source volume. Longitudinally, the mesa is assumed to reach 100 nm below the oxide position; radially, a region up to 10 μm beyond the oxide aperture is embedded in a passivation material.

The solver takes as inputs the thermal conductivity map κ of the VCSEL (whose values are summarized in Tab. 1) and the heat sources profile Q, related to the oxide shape. From a quantitative standpoint, the heat equation computes the inner temperature variation T by solving:

$$\nabla \cdot [\kappa(x, y, z)\nabla T(x, y, z)] = -Q(x, y, z), \tag{13}$$

At the substrate side, a Dirichlet boundary condition $T(x, y, 0) = T_a$ is imposed, where T_a is the ambient temperature assumed to be 300 K unless otherwise stated.

Precise heat sources are only available through a self-consistent solution of transport and optical problems, as in our VENUS suite, which is currently outside our scope. We have therefore tackled the issue differently, but grounding our approach as much as possible on VENUS. Within this scope, we use analytical heat source distributions, related to the oxide aperture position and size, to achieve a best fit with VENUS temperature profiles. This is shown in Fig. 4(a)-(b), with the heat source dependence in the longitudinal and transverse directions, respectively. The former consists of piecewise exponential dependence, with the addition of a peak due to the highly absorbing PML. Transversally, we adopt a Gaussian profile; all parameters are directly related to the oxide aperture radius and longitudinal position.

Then, we derive the dissipated power P_{diss} from the LIV characteristics as

$$P_{\text{diss}}(I) = IV - P, \tag{14}$$

where V and P indicate the bias voltage and the output optical power. Fixing a bias current I, the corresponding $Q(x, y, z)$ volume integral is set to the dissipated power $P_{\text{diss}}(I)$. Neglecting thermal nonlinearities, we compute the thermal profile only once for a given P_{diss} and rescale it according to the VCSEL operation point. In summary, once $P_{\text{diss}}(I)$ is known, $\Delta T(I)$ follows directly.

Optics EXPRESS

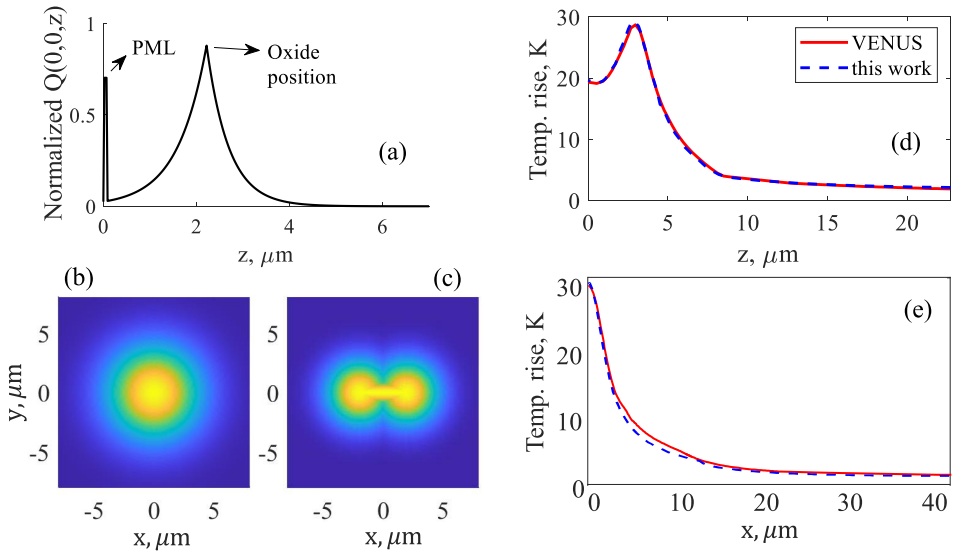

Fig. 4. (a) Longitudinal profile of the heat source employed in the thermal solver. (b-c) Transverse profiles of the heat source at the AR in the circular and ABT case, respectively. (d)-(e) comparison of the self-heating temperature profile obtained from our fitted heat source and with VENUS detailed sources [32].

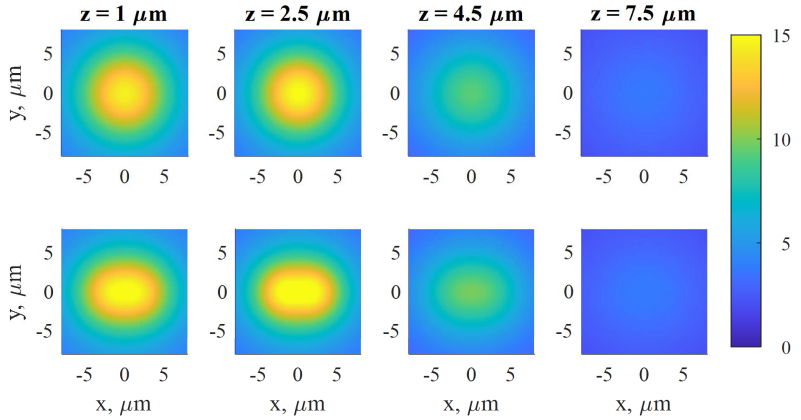

Fig. 5. Transverse self-heating temperature profiles in °C obtained at a P_{diss} = 5 mW in the circular case (first row) and the BT case (second row) at different longitudinal coordinates.

In Fig. 4(d)–(e), we compare the longitudinal and transverse temperature profile cuts obtained with the analytically shaped heat sources to the same quantities computed from the detailed sources of VENUS. Then, we apply it to the ABT-VCSEL, retaining the same longitudinal dependence. Radially, the profile is adapted to the BT geometry (Fig. 4(c)): at the apertures, two radially decaying Gaussian functions are centered; at the bridge, another Gaussian –whose peak is located along the horizontal symmetry axis– decays along $|y|$.

Figure 5 compares temperature transverse cuts at various longitudinal sections for the two analyzed oxide aperture shapes: circular and bow-tie. For the ABT-VCSEL, temperature assumes stadium-like shapes instead of the circularly symmetrical cuts of the standard VCSEL with the same area.

Optics EXPRESS

4. Results and discussion

We apply our suite for the design of the ABT-VCSEL which minimizes the impact of technological variations while allowing for bandwidth enhancement. To do so, we consider the nominal structure described in Section 2 and we vary the applied current and PML thickness. Then, we proceed to asymmetrize the BT aperture to asses robustness to oxide asymmetries, to change the ambient temperature and, finally, to vary dynamical parameters such as linewidth enhancement factor and ϵ_{nlg}.

The modal field distributions, *i.e.*, $\Psi_1(x, y)$ and $\Psi_2(x, y)$, at the AR of the ABT-VCSEL are crucial to understand its dynamical properties. For PML = 50 nm and current 5.5 mA, the corresponding mode profiles are shown in Fig. 6(a)–(f). It can be observed that $|\Psi_1|^2$ resembles an even mode (mode #1), whereas $|\Psi_2|^2$ resembles an odd one (mode #2). However, due to the transversely patterned reflectivity, both modes are intrinsically complex (*i.e.*, they cannot be made purely real through multiplication by a complex constant) in contrast to the perfectly symmetric case of [23]. Their product $\Psi_1^*\Psi_2$ is a fundamental ingredient for our ABT-VCSEL operation, because it enables PPR. Therefore, we report at the bottom of Fig. 6 the corresponding real and imaginary parts. The former exhibits an even distribution (g), while the latter (h) displays an odd one. This also indicates that the modes are not orthogonal and that ξ_{12}, defined in (6), is mostly real. As a consequence, the cross-power term in (5) provides a significant contribution, underlying the importance of the discussion for a correct evaluation of the output power $P(t)$, as derived in the Supplement 1.

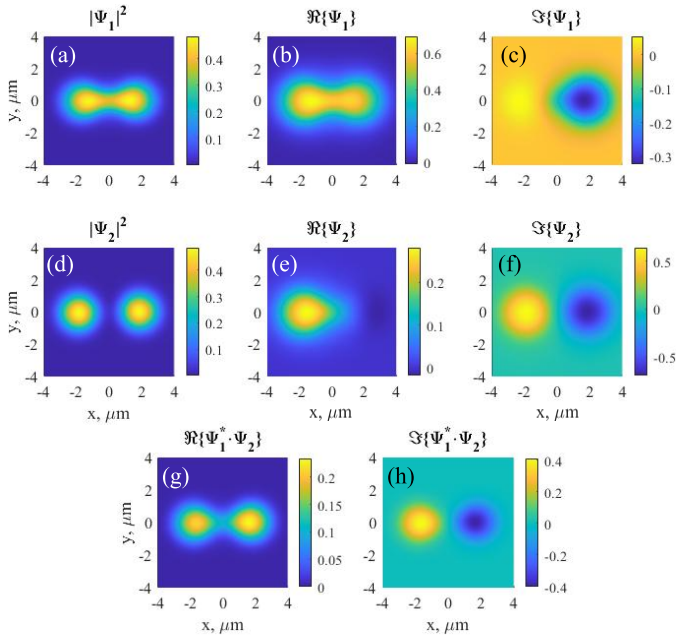

Fig. 6. Fundamental and first-order modes (Ψ_1 and Ψ_2) of the ABT-VCSEL at the AR section, shown as squared modulus (a-d), real part (b-e), and imaginary part (c-f). Panels (g) and (h) display the real and imaginary parts of the product $\Psi_1^* \cdot \Psi_2$. In this example, I = 5.5 mA and the PML thickness was fixed at 50 nm. Both Ψ_1 and Ψ_2 are reported in arbitrary units, however they are normalized in the same way, so that the color bars are comparable.

Let's discuss the optical simulations results at varying PML thickness and current (*i.e.*, temperature profile correspondingly) for both the ABT-VCSEL and of its reference circular

Optics EXPRESS

counterpart. The relevant modal parameters are reported in Fig. 7, comparing the fundamental mode features of the circular case (Fig. 7(a-b-c)) with those of the ABT-VCSEL (Fig. 7(d-e-f)). Frequency splitting Δf and threshold gain relative difference Δg reported in Fig. 7(g–h) are defined as:

$$\Delta f = c\left(\frac{1}{\lambda_2} - \frac{1}{\lambda_1}\right), \quad \Delta g = 100 \cdot \frac{G_{\text{th}}^{(2)} - G_{\text{th}}^{(1)}}{G_{\text{th}}^{(1)}}. \tag{15}$$

In the case of the circular VCSEL, threshold gain and outcoupling efficiency are current-independent, while extremely sensitive to PML thickness (Fig. 7(b–c)). In fact, at around 100 nm the reflection is nearly in antiphase and the threshold strongly increases [39].

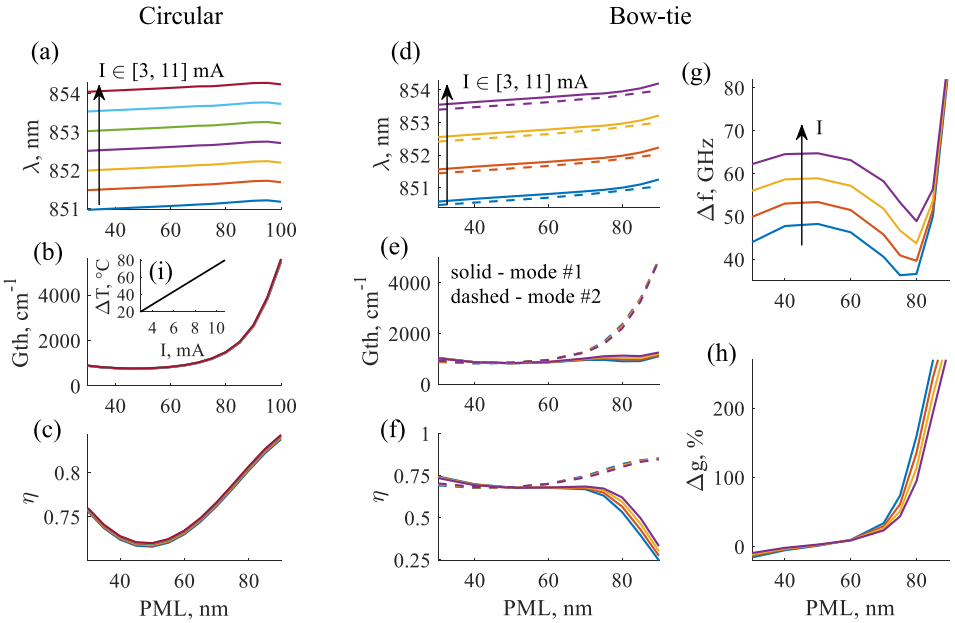

Fig. 7. Summary of the optical results for both structures, shown as a function of the PML thickness and current. Inset (i) shows how the current is linearly linked to the self-heating temperature ΔT. The first column represents (a) the emission wavelength, (b) threshold gain and (c) outcoupling efficiency of the fundamental mode in the circular case. Similarly, the second column (d-e-f) shows the same quantities for the ABT case. Solid and dashed lines refer to the fundamental and to the first-order mode, respectively. Finally, the last column shows the frequency spacing Δf (g) and the relative threshold gain difference Δg (h) between the two modes.

The interpretation of Fig. 7(e) in the ABT case is more involved. The threshold gain of mode #2 with PML up to 60 nm is comparable to the circular case, despite the reduced number of semiconductor top DBR pairs (from 20 to 17). This is due to the additional reflectivity provided by the hollowed dielectric DBR. To explain why $G_{\text{th}}^{(2)}$ increases with thicker PMLs, let us consider the distribution of $|\Re\{S_z(x, y = 0, z)\}|$ within the ABT-VCSEL for both modes and for three PML values of Fig. 8. For $z>0$ ($z = 0$ corresponds to the outcoupling facet) the power exits only through the dielectric DBR hole. For PML = 20 and 50 nm (Fig. 8(a-b-c-d)), the optical power inside the VCSEL is nearly even in the two apertures, resulting in a relatively small Δg and low values of $G_{\text{th}}^{(1)}$ and $G_{\text{th}}^{(2)}$, since both modes benefit from the increased reflectivity of the dielectric DBR. For a PML of 80 nm, (Fig. 8(e)), the mode #1 remains distributed across both apertures, leaving its threshold gain nearly unaffected. In contrast, the mode #2 becomes strongly localized

Optics EXPRESS

to the right aperture (note the logarithmic colour scale in Fig. 8(f)), directly beneath the DBR hole. Additionally, the reflectivity of the top semiconductor DBR is significantly reduced for PML = 80 nm, leading to a larger $G_{\text{th}}^{(2)}$, as also occurs with the circular VCSEL. Consequently, the odd mode features a comparable outcoupling efficiency, while that of the even mode drastically drops, as shown in Fig. 7(f). Concerning the oscillations shown in Fig. 8, they arise from the sign change of the Poynting vector and are further accentuated by the logarithmic representation.

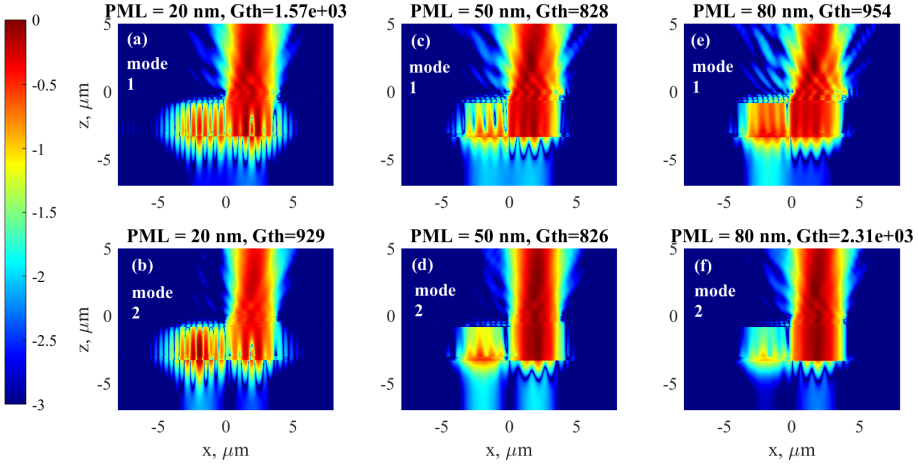

Fig. 8. Normalized logarithmic distribution of S_z in the (x, z) plane for PML thicknesses of 20 nm (a-b), 50 nm (c-d), and 80 nm (e-f), for fundamental mode (a-c-e) and the first-order mode (b-d-f) of the ABT-VCSEL. The corresponding threshold gain G_{th} is also reported, expressed in cm^{-1}.

We apply now our dynamical model (4)–(3), for which we choose a linearized carrier recombination model: $R(N) = N/\tau_n$, with the carrier lifetime τ_n in Table 1. By applying a current pulse on top of the steady-state bias current, via a post-processing of the corresponding $P(t)$ computed through (5) [23], we obtain an IM response for each current and for each PML value. For each IM response, we define its bandwidth $f_{3\text{dB}}$ as the first intersection between the IM response and the -3 dB level, and its modulation swing as its maximum range in dB for frequencies from 0 to $f_{3\text{dB}}$. A high modulation swing is detrimental for large-signal modulation, and, according to our definition, its lower bound is set to 3 dB.

These quantities are reported in Fig. 9 for the circular case, showcasing a maximum bandwidth of 38 GHz. Both $f_{3\text{dB}}$ and the modulation swing have the expected dependency on applied current [35].

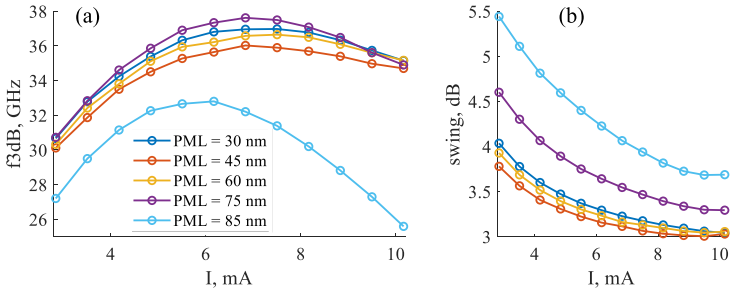

Fig. 9. $f_{3\text{dB}}$ and modulation swing in the circular case as a function of current, shown for some of the PML thicknesses.

Optics EXPRESS

Fixing the current at 6.8 mA, the corresponding f_{3dB} is plotted against PML in Fig. 10(a) and against the photon lifetime τ_p in Fig. 10(b). The latter is obtained from Fig. 7(b) and (1). The non-monotonic trend is confirmed by experimental data published in [6] and reported in the inset 7(c), showing how our simulation workflow describes the VCSEL dynamical behaviour starting only from the VCSEL structure. It should be noted that our model addresses only the intrinsic modulation bandwidth of the laser, without accounting for additional parasitic effects, as these lie beyond the scope of this work. The parasitic contributions affecting the investigated device are expected to be comparable to those of conventional VCSELs.

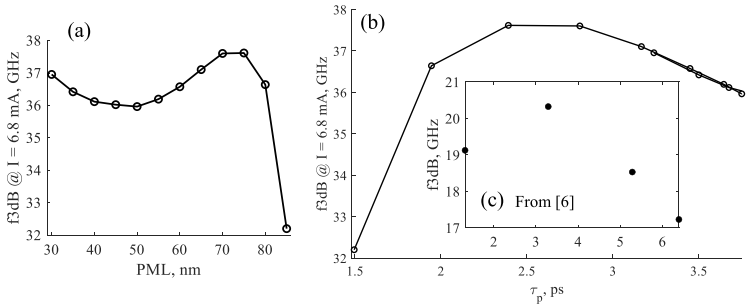

Fig. 10. f_{3dB} at I = 6.8 mA in the circular case, as a function of the PML thickness (a) and the photon lifetime (b). The inset (c) reports the experimental data in [6] for a circular VCSEL, showing a trend similar to simulations.

Similarly, bandwidth and modulation swing as functions of current and PML in the ABT-VCSEL are reported in Fig. 11, showing a staggering improvement of its bandwidth. For each PML we select the current that provides the largest f_{3dB} and plot such best cases in Fig. 12(a), which shows that f_{3dB} reaches 70 GHz with a very low modulation swing at PML = 50 nm. For each data point of Fig. 12(a), the corresponding IM responses are reported in Fig. 12(b). One can see how the bandwidth enhancement up of 70 GHz is due to the PPR peak being above the −3 dB line; however, even when it is below such high value, f_{3dB} remains significantly higher than in the circular case. The PPR peak occurs approximately at the frequency separation Δf [23]. Since this quantity is strongly dependent on the thermal lensing and therefore on current, as shown in Fig. 7(g), an accurate evaluation of temperature is crucial. Moreover, a further correction originates from the imaginary part of the optical gain associated with a nonzero linewidth enhancement factor α, as given in (9).

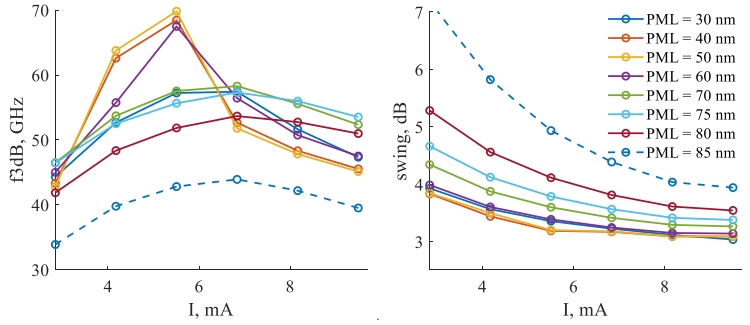

Fig. 11. (a) f_{3dB} and (b) modulation swing in the ABT case as a function of current, for several PML thicknesses.

The comparison between circular and ABT-VCSELs performance is reported in Fig. 13. Panel 13(a) displays the best bandwidth across all currents as a function of the PML thickness in the two

Optics EXPRESS

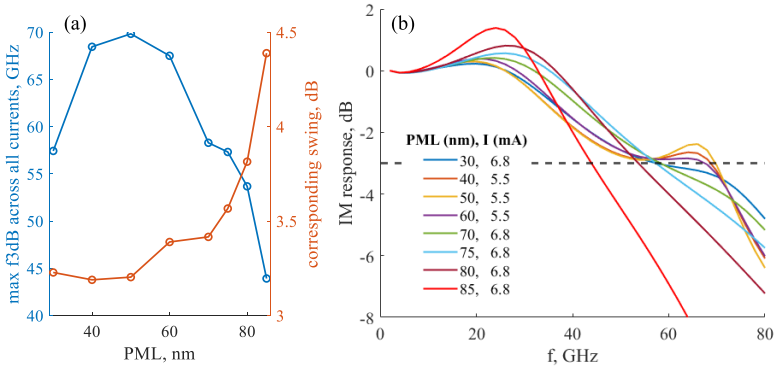

Fig. 12. (a) Maximum f_{3dB} across all considered currents as a function of the PML thickness and corresponding modulation swing in the ABT case. (b) IM responses associated to all points of panel (a). The horizontal black dashed line represents the −3 dB level. At PML thicknesses of 40, 50 and 60 nm the PPR peak rises above −3 dB.

cases, while panels 13(b)–(e) show the eye diagrams obtained via pulse-amplitude modulation with a random bit sequence employing two current levels (PAM-2), set to 2 and 9 mA. When the modulation frequency is set to 70 GHz, both structures still feature an open eye, although at 100 GHz only the eye associated with the ABT-VCSEL remains open. Aiming at a higher bit rate, Fig. 14 shows the comparison of a 70 GHz PAM-4 modulation for the circular (a) and ABT (b) device with four current levels equally spaced between 2 and 9 mA. It can be seen that in the ABT case the eyes are still opened, further confirming the advantages of the ABT-VCSEL with respect to the circular one, making our device a good candidate for the next generation high-speed VCSELs. However, the PAM-4 ABT eye diagram features detrimental distortion effects, which prevents going to higher modulation frequencies in the PAM-4 scheme. These latter, however, might be mitigated by predistortion techniques [15], which is beyond the scope of this work.

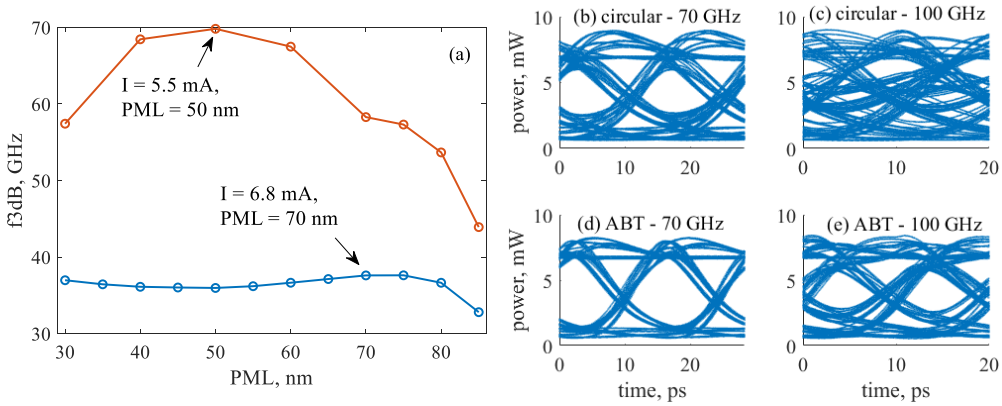

Fig. 13. Comparison of the dynamic performance between circular and ABT-VCSEL. (a) Maximum f_{3dB} for both designs. For the PAM-2 eye-diagram analysis, the PML thickness is fixed at 70 nm for the circular case and 50 nm for the ABT case, with two current levels set to 2 and 9 mA, respectively. Panels (b) and (c) show the circular VCSEL PAM-2 eye diagrams under direct modulation at 70 GHz, where the eye remains open, and at 100 GHz, where it closes. Panels (d) and (e) display the PAM-2 ABT-VCSEL eye diagrams at the same frequencies, with the eye remaining open even at 100 GHz.

Optics EXPRESS

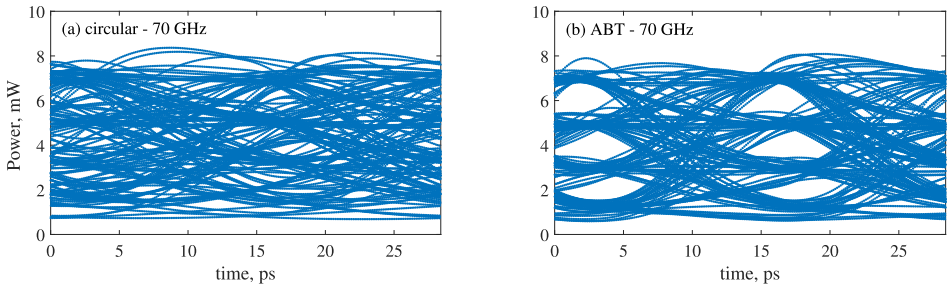

Fig. 14. PAM-4 eye diagrams for both the circular (a) and the ABT (b) VCSELs with four current levels equally spaced between 2 and 9 mA, with a frequency of 70 GHz.

We now assess the robustness of the obtained results to variations in both modal and material parameters. The modal parameters are not independent variables, as they are determined by the device geometry; consequently, their variation must be introduced through corresponding modifications of the structural design. Previous studies [24] have demonstrated that oxide asymmetries can strongly affect the modal properties, motivating a detailed investigation of this effect in the present analysis. For instance, we fix PML = 50 nm and $R_2 = 1.5\,\mu$m, and vary the radius of the left aperture R_1 around the nominal value of 1.5 μm. The resulting maximum bandwidth as a function of R_1 is shown in Fig. 15(a), with the corresponding IM responses reported in panel 15(b). The analysis shows that variations of several hundred nanometers relative to the symmetric case $R_1 = R_2 = 1.5\,\mu$m are acceptable while still ensuring high-speed performance. When exiting the stability range, it can be observed from panel 15(b) that as R_1 decreases, the PPR peak drops below −3 dB, whereas increasing R_1 drives the system towards a beating regime. In more mature edge-emitter PPR implementations, additional tuning elements are often incorporated to compensate for unavoidable fabrication-induced variations [40]. A similar concept could be applied here to mitigate the detrimental effects of oxide asymmetries by employing a lateral heating approach, which has been previously implemented in [41] and could be investigated in future work. We also investigated the effect of an isotropic scaling of the symmetrical BT aperture, finding that the proposed ABT-VCSEL can tolerate oxides deviating of ±200 nm from the nominal dimensions.

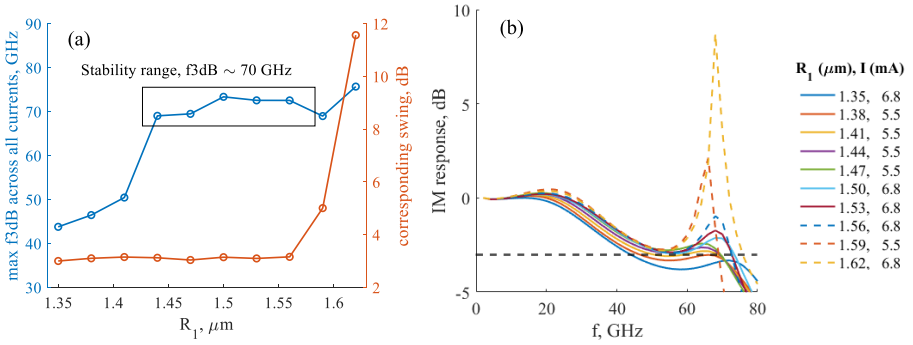

Fig. 15. (a) Maximum $f_{3\mathrm{dB}}$ across all currents, together with the corresponding modulation swing, as a function of R_1 and (b) associated IM responses.

Finally, we test the robustness of our ABT-VCSEL with respect to other model parameters, such as ambient temperature, the Henry α-factor, and the non-linear gain coefficient, which may vary depending on the QW design.

Optics EXPRESS

Up to this point, the ambient temperature T_a has been kept at 300 K. We now test our device for T_a = 300 K, which is a more realistic scenario in a datacenter environment. Results are reported in Fig. 16 as blue curves, where the LI characteristics (a) and best IM responses (b) are compared to the room temperature case (black curves). As expected, rising the ambient temperature is detrimental to both the maximum optical power and f_{3dB}, as the PPR peak drops well below −3 dB. However, it is possible to retrieve PPR-enhanced performance by properly engineering the cavity detuning $\Delta\lambda$ [32]. For increasing values of $\Delta\lambda$ we observe that the LI characteristics reach values comparable to the room temperature case. Similarly, the PPR peak gets closer to −3 dB, leaving room for possible optimization. In fact, all curves appear to be equalizable [15,42], except for the blue one in Fig. 16(b) ($\Delta\lambda$ = 0, I = 4.2 mA), which shows an excessively steep roll-off after ∼ 30 GHz. The other responses, despite notches of about 3-5 dB and mild resonances, remain suitable for compensation through standard electronic post- or pre-equalization techniques such as feed-forward equalizers (FFE), which can flatten the frequency response and mitigate intersymbol interference. We will not enter this field, because it is out of our scope, but it is worth underlining the further potential of our ABT-VCSEL design when applying such methodologies.

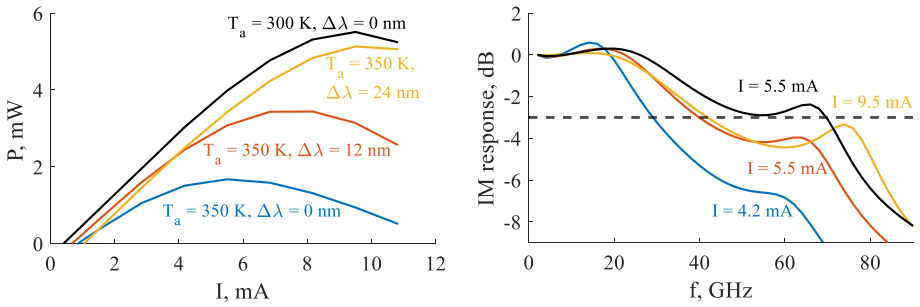

Fig. 16. (a) Effect of ambient temperature on the LI characteristics of the ABT-VCSEL and (b) on the best IM responses, for different values of cavity detuning $\Delta\lambda$.

As a final verification, we varied the dynamical parameters α_H and ϵ_{nlg} around their typical values reported in Table 1. The corresponding IM responses, shown in Fig. 17, exhibit a smooth dependence on both parameters. This demonstrates that uncertainties about their exact values affect in a limited way the performance of our device. Again, post- or pre-equalization techniques might compensate for such variations.

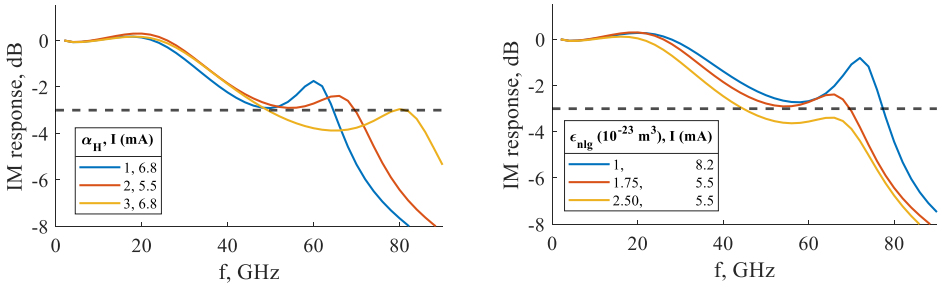

Fig. 17. Impact of α_H (a) and ϵ_{nlg} (b) on the best IM responses.

5. Conclusions

In this paper, we focus on the PPR as an enabler of next-generation ultra-fast optical sources to meet the growing demand from datacenters. We have developed a VCSEL dynamical suite

Optics EXPRESS

and successfully tested it on experimental results. Supported by this, we have deployed it to introduce the concept and design of ABT-VCSELs, aiming to overcome the limitations of standard BT-VCSELs evidenced by our previous works.

Our proposal eliminates the need for asymmetric pumping and/or selective probing, which has made the symmetric bow-tie concept unattractive for mass application. It is based on a hollowed dielectric DBR applied above one of the two bow-tie apertures, which enables strong modal coupling under uniform carrier injection. The results of combined electromagnetic, thermal and dynamical simulations suggest that ABT-VCSELs can achieve small-signal bandwidths up to 70 GHz at significant output power, and sustain open PAM-2 eyes at 100 GHz. Compared to standard circular VCSELs, this represents a significant advance, almost doubling its performance. Robustness analysis supports tolerance to geometric variations of the oxide aperture, as well as the possibility of mitigating ambient temperature degradation through cavity detuning. These results highlight ABT-VCSELs as a promising device for next-generation short-reach interconnects, combining ultrafast direct modulation with fabrication-friendly design.

Funding. NextGenerationEU (PE00000001 Program RESTART, Project RIGOLETTO, CUP E63C22002040007).

Acknowledgment. This work was partially supported by Cisco Systems through the ULTRA-VCSELs research contract and NRRP, NextGenerationEU (CUP E63C22002040007) Grant PE00000001 Program RESTART, Project RIGOLETTO. This work was performed within VCSELence, a collaborative framework at the Politecnico di Torino Campus, involving CNR, DET and Links Foundation.

Disclosures. The authors declare no conflicts of interest.

Data availability. Data underlying the results presented in this paper are not publicly available at this time but may be obtained from the authors upon reasonable request.

Supplemental document. See Supplement 1 for supporting content.

References

1. A. Liu, P. Wolf, J. A. Lott, *et al.*, "Vertical-cavity surface-emitting lasers for data communication and sensing," Photonics Res. **7**(2), 121–136 (2019).
2. B. D. Padullaparthi, J. A. Tatum, and K. Iga, eds., *VCSEL industry - Communication and sensing* (John Wiley & Sons, Hoboken (NJ), 2022), 1st ed.
3. N. N. Ledentsov, O. Y. Makarov, V. A. Shchukin, *et al.*, "High speed VCSEL technology and applications," J. Lightwave Technol. **40**(6), 1749–1763 (2022).
4. M. Srinivasan, J. Song, A. Grabowski, *et al.*, "End-to-end learning for VCSEL-based optical interconnects: State-of-the-art, challenges, and opportunities," J. Lightwave Technol. **41**(11), 3261–3277 (2023).
5. P. Westbergh, J. S. Gustavsson, B. Kögel, *et al.*, "Higher speed VCSELs by photon lifetime reduction," in *Vertical-Cavity Surface-Emitting Lasers XV*, vol. 7952 J. K. Guenter and C. Lei, eds., International Society for Optics and Photonics (SPIE, 2011), p. 79520K.
6. P. Westbergh, J. S. Gustavsson, B. Kogel, *et al.*, "Impact of photon lifetime on high-speed vcsel performance," IEEE J. Select. Topics Quantum Electron. **17**(6), 1603–1613 (2011).
7. E. Haglund, P. Westbergh, J. S. Gustavsson, *et al.*, "High-speed vcsels with strong confinement of optical fields and carriers," J. Lightwave Technol. **34**(2), 269–277 (2016).
8. M. D'Alessandro, A. Gullino, A. Tibaldi, *et al.*, "Physics-based time-domain modeling of vcsels," in *2022 International Conference on Numerical Simulation of Optoelectronic Devices (NUSOD)*, (2022), pp. 61–62.
9. A. Larsson, J. S. Gustavsson, A. Fülöp, *et al.*, "The future of VCSELs: Dynamics and speed limitations," in *2020 IEEE Photonics Conference (IPC)*, (2020).
10. H.-T. Cheng, Y.-C. Yang, T.-H. Liu, *et al.*, "Recent advances in 850 nm vcsels for high-speed interconnects," Photonics **9**(2), 107 (2022).
11. J. Wang, M. V. R. Murty, S. Jiang, *et al.*, "200Gb/s PAM4 oxide VCSEL development progress at Broadcom," in *Vertical-Cavity Surface-Emitting Lasers XXIX*, vol. 13384 K. D. Choquette and L. A. Graham, eds., International Society for Optics and Photonics (SPIE, 2025), p. 1338403.
12. D. M. Kuchta, A. V. Rylyakov, C. L. Schow, *et al.*, "A 50 Gb/s NRZ modulated 850 nm VCSEL transmitter operating error free to 90 °c," J. Lightwave Technol. **33**(4), 802–810 (2015).
13. J. Zhang, P. Gou, M. Kong, *et al.*, "PAM-8 IM/DD transmission based on modified lookup table nonlinear predistortion," IEEE Photonics J. **10**(6), 1–9 (2018).
14. H. Zhou, Y. Li, Y. Liu, *et al.*, "Recent advances in equalization technologies for short-reach optical links based on PAM4 modulation: A review," MDPI Appl. Sci. **9**(11), 2342 (2019).
15. L. Minelli, F. Forghieri, A. Nespola, *et al.*, "A multi-rate approach for nonlinear pre-distortion using end-to-end deep learning in IM-DD systems," J. Lightwave Technol. **41**(2), 420–431 (2023).

Optics EXPRESS

16. M. Lindemann, G. Xu, T. Pusch, *et al.*, "Ultrafast spin-lasers," Nature **568**(7751), 212–215 (2019).
17. L. Marigo-Lombart, C. Viallon, A. Rumeau, *et al.*, "Electro-absorption modulator vertically integrated on a vcsel: Microstrip-based high-speed electrical injection on top of a bcb layer," J. Lightwave Technol. **37**(15), 3861–3868 (2019).
18. S. T. M. Fryslie, Z. Gao, H. Dave, *et al.*, "Modulation of coherently coupled phased photonic crystal vertical cavity laser arrays," IEEE J. Select. Topics Quantum Electron. **23**(6), 1–9 (2017).
19. E. Heidari, H. Dalir, M. Ahmed, *et al.*, "Hexagonal transverse-coupled-cavity VCSEL redefining the high-speed lasers," Nanophoton. **9**(16), 4743–4748 (2020).
20. W. North, N. Jahan, P. Strzebonski, *et al.*, "Analysis and characterization of photon-photon resonance in coupled dual-element photonic crystal vertical cavity surface emitting laser arrays," J. Lightwave Technol. **42**(1), 236–242 (2024).
21. H. Dalir and F. Koyama, "Bandwidth enhancement of single-mode VCSEL with lateral optical feedback of slow light," IEICE Electron. Express **8**(13), 1075–1081 (2011).
22. D. Chen, Y. Liu, and Y. Yu, "Understanding the photon-photon resonance of DBR lasers using mode expansion method," Opt. Quantum Electron. **55**(1), 29 (2023).
23. M. D'Alessandro, V. Torrelli, F. Bertazzi, *et al.*, "Transverse coupled cavity vcsels: Bridging ultrabroadband dynamics to optical supermodes," IEEE Photonics J. **16**(2), 1–7 (2024).
24. M. Lindemann, M. D'Alessandro, N. Ledentsov, *et al.*, "Laterally coupled vertical-cavity surface-emitting lasers with tunable resonance width and frequency," J. Appl. Phys. **138**(5), 053102 (2025).
25. M. D'Alessandro, V. Torrelli, P. Debernardi, *et al.*, "Modelling coherent emission in transverse coupled cavity vcsels," in *NUSOD 2025*, (2025).
26. N. Ledentsov Jr., V. A. Shchukin, L. Chorchos, *et al.*, "Analysis of laterally-coupled-cavity VCSELs for ultra-high-frequency photon-photon resonance modulation," in *Vertical-Cavity Surface-Emitting Lasers XXVIII*, vol. 12904 C. Lei and K. D. Choquette, eds., International Society for Optics and Photonics (SPIE, 2024), p. 1290405.
27. M. Lindemann, N. C. Gerhardt, M. Hofmann, *et al.*, "Coupled aperture VCSELs suitable for 100 GHz intensity modulation," in *2023 23rd International Conference on Transparent Optical Networks (ICTON)*, (2023).
28. V. Torrelli, M. Alasio, M. D'Alessandro, *et al.*, "Modelling self-heating in high-power single-mode phase-coupled linear vcsel arrays," IEEE Photonics Journal (2025).
29. G. P. Bava, P. Debernardi, and L. Fratta, "Three-dimensional model for vectorial fields in vertical-cavity surface-emitting lasers," Phys. Rev. A **63**(2), 023816 (2001).
30. V. Torrelli, "Vertical-cavity surface-emitting lasers: Computer-aided modal and polarization engineering," Phd thesis, Politecnico di Torino (2025).
31. M. D'Alessandro, N. Ledentsov Jr., V. A. Shchukin, *et al.*, "Physics-based computer-aided modelling of transverse coupled cavity VCSELs," in *Vertical-Cavity Surface-Emitting Lasers XXIX*, vol. PC13384 K. D. Choquette and L. A. Graham, eds., International Society for Optics and Photonics (SPIE, 2025), p. PC1338405.
32. A. Tibaldi, F. Bertazzi, M. Goano, *et al.*, "VENUS: a Vertical-cavity surface-emitting laser Electro-opto-thermal NUmerical Simulator," IEEE J. Select. Topics Quantum Electron. **25**(6), 1–12 (2019).
33. V. Torrelli, L. Miri, M. D'Alessandro, *et al.*, "Elliptical polarization in vcsels via joint interaction of a tilted sub-wavelength grating and intrinsic semiconductor anisotropies," Opt. Lett. **50**(9), 3082–3085 (2025).
34. L. Fu, N. Cui, F. Zhang, *et al.*, "Ultrahigh polarization-stable narrow-linewidth grating coupled-cavity vertical-cavity surface-emitting laser for atomic clock systems," Opt. Express **33**(16), 34294–34302 (2025).
35. L. A. Coldren and S. W. Corzine, *Diode Lasers and Photonic Integrated Circuits* (John Wiley & Sons, New York, 1995).
36. F. Prati, A. Tesei, L. A. Lugiato, *et al.*, "Stable states in surface-emitting semiconductor lasers," Chaos Solitons Fractals **4**(8-9), 1637–1654 (1994).
37. P. Debernardi, A. Tibaldi, M. Daubenschüz, *et al.*, "Probing thermal effects in VCSELs by experiment-driven multiphysics modeling," IEEE J. Select. Topics Quantum Electron. **25**(6), 1–14 (2019).
38. M. C. G. Alasio, V. Torrelli, S. Albano, *et al.*, "Modeling self-heating in high-power non-circular vcsels," in *2024 IEEE Photonics Conference (IPC)*, (2024), pp. 1–2.
39. V. Torrelli, A. Gullino, A. Tibaldi, *et al.*, "High-power emission via large-area vcsels with single high-order mode operation," IEEE Photonics J. **16**(2), 1–7 (2024).
40. A. Zozulia, R. Schatz, S. Rihani, *et al.*, "C-band directly modulated lasers with tunable photon–photon resonance in inp membrane," IEEE J. Quantum Electron. **60**(6), 1–12 (2024).
41. T. Pusch, E. La Tona, M. Lindemann, *et al.*, "Monolithic vertical-cavity surface-emitting laser with thermally tunable birefringence," Appl. Phys. Lett. **110**(15), 151106 (2017).
42. P. Torres-Ferrera, G. Rizzelli, A. Nespola, *et al.*, "Statistical analysis of 100 gbps per wavelength swdm vcsel-mmf data center links on a large set of om3 and om4 fibers," J. Lightwave Technol. **40**(4), 1018–1026 (2022).